ELSEVIER

Materials Science and Engineering B97 (2003) 265–274

MATERIALS SCIENCE & ENGINEERING B

www.elsevier.com/locate/mseb

Investigation of the physical properties of a blue-emitting phosphor produced using a rapid exothermic reaction

E.J. Bosze [a], J. McKittrick [a,*], G.A. Hirata [a,b]

[a] *Materials Science and Engineering Program, Department of Mechanical and Aerospace Engineering, University of California at San Diego, Building EBU II, 9500 Gilman Drive, La Jolla, CA 92093-0411, USA*

[b] *Centro de Ciencias de la Materia Condensada, Universidad Nacional Autónoma de México, Ensenada, Baja California, C.P. 22860, Mexico*

Received 26 June 2002; received in revised form 11 November 2002; accepted 25 November 2002

Abstract

The blue-emitting phosphor cerium activated yttrium silicate, $(Y_{1-m}Ce_m)_2SiO_5$, was prepared via a novel synthesis technique called combustion synthesis. Combustion synthesis involves a highly exothermic redox reaction between metal nitrates and an organic fuel to produce a solid powder. The combustion synthesis parameter, the fuel-to-oxidizer ratio, has a direct effect on the physical properties of the as-synthesized powders due to the reaction temperature being dependent on the variation of this ratio. Thus, varying the fuel-to-oxidizer ratio produced powders with varying crystallite sizes, carbon contamination and surface areas, which in turn affected the luminescent efficiencies of the as-synthesized powders. The reaction temperature was found to reach a maximum with a 60% fuel rich mixture, with the powders exhibiting the largest crystallite sizes, smallest surface area and carbon contamination, and highest luminescent efficiency in the as-synthesized state. As-synthesized powders exhibit a high degree of porosity due to the large amount of gas to solid formed. To more accurately predict the specific surface areas of porous powders, the standard geometrical model used for gas absorption measurements was modified for porous particles and found to more accurately predict the specific surface area of highly porous powders.

Keywords: Combustion synthesis; Phosphor; Fuel-to-oxidizer ratio; Surface ratio

1. Introduction

Luminescent materials (phosphors) have extensive use in the lighting and display industries. Phosphor powders are usually produced via solid state synthesis techniques. This requires mixing, grinding and annealing the starting constituents at high temperatures, >1600 °C, for long periods of time to produce phosphor powders with satisfactory properties, such as small particle sizes, high crystallinity and homogeneity, and phase purity. It is necessary for phosphor powders to exhibit these satisfactory properties to achieve high efficiency luminescence. Often, solid state synthesized phosphors contain unreacted constituents and other metal contaminants that harm the luminescent properties. An alternative, lower temperature synthesis technique of combustion synthesis produces powder using an exothermic reaction between metal nitrates and an organic fuel. It has been shown to produce fine particle oxide ceramic powders, such as Al_2O_3 and phosphor powders, such as Y_2O_3:Eu and $BaMg_2Al_{10}O_{17}$:Eu [1–4]. Combustion-synthesized phosphors that often exhibit these satisfactory properties, require only short high temperature annealing schedules to achieve high efficiency luminescence [4,5]. The focus of this study is to quantitatively determine the effect of a combustion synthesis parameter, the fuel-to-oxidizer ratio (f/o), on the physical properties of a candidate blue-emitting phosphor, cerium activated yttrium silicate $(Y_{1-m}Ce_m)_2SiO_5$, in the as-synthesized state. Crystallite sizes, phases, morphology, surface area and carbon contamination were all determined for each f/o and then the effect of these physical properties were related to the cathodoluminescent properties of as-synthesized phosphor.

* Corresponding author. Tel.: +1-858-534-5425; fax: +1-858-534-5698.

E-mail address: jmkittrick@ucsd.edu (J. McKittrick).

0921-5107/02/$ - see front matter
doi:10.1016/S0921-5107(02)00598-6

Eq. (1) shows a chemically balanced, stoichiometric combustion synthesis reaction that produces the studied material, Y_2SiO_5, from yttrium nitrate ($Y(NO_3)_3$), SiO_2 and carbohydrazide (CH_6N_4O). The heat of reaction, ΔH_{rxn}, calculated from this reaction at 298 K is -2286.3 kJ mol^{-1} (see Table 1 for ΔH_f^o).

$$2Y(NO_3)_3 + 1SiO_2 + \frac{15}{4}\ CH_6N_4O \rightarrow Y_2SiO_5 + \frac{45}{4}\ H_2O + \frac{15}{4}\ CO_2 + \frac{21}{2}\ N_2 \quad (1)$$

Normally, constituent oxides are mixed, ground and fired in a high temperature furnace in excess of 1600 °C to produce the above multiconstituent oxide. In combustion synthesis, the redox reaction itself produces the high temperatures required to fabricate this oxide. Reactants are dissolved in solution that is boiled at ≈ 500 °C and spontaneously burst into flames. The reaction is self-propagating and can produce temperatures in excess of 1500 °C long enough (≈45 s for the reaction to come to completion) to synthesize the desired product. As the flame propagates in the reaction vessel, a solid powder grows, while inert gases, such as H_2O, CO_2 and N_2, are also released, which create porosity in the growing powder. In the end, the reaction yields a porous mass of powder with a large surface area, that fills the volume of the reaction vessel [4].

A combustion synthesis reaction can be influenced by several parameters, such as the type of fuel, fuel-to-oxidizer ratio (f/o), the water content of the precursor mixture and the ignition temperature [5]. In this study, the effects of the f/o parameter were investigated. Varying the f/o has a direct effect on the reaction or flame temperature, which in turn has an effect on the physical properties of the as-synthesized powders. Details on the calculation of the f/o can be found in Ref. [4].

Table 1
The enthalpies of formation and heat capacities of the reactants and products [18] at 298.15 K

Compound	ΔH_f^o(298.15 K) (kJ mol^{-1})	C_p (T) (J mol^{-1} K)#
$Y(NO_3)_3$	−1424	
SiO_2	−911	
CH_6N_4O	−277	
Y_2SiO_5	−2869†	122*
H_2O (gas)	−243	$30+10.71\times10^{-3}T+0.33\times10^{5}/T^2$
N_2	0	$27.87+4.27\times10^{-3}T$
CO_2	−395	$44.14+9.04\times10^{-3}T-8.54\times10^{5}/T^2$
CO	−114	$28.41+4.10\times10^{-3}T-0.46\times10^{5}/T^2$
O_2	0	$29.96+4.18\times10^{-3}T-1.67\times10^{5}/T^2$

* Estimated from Al_2SiO_5, andalusite, [18].
† Ref. [19].
# Heat capacities from Ref. [20].

The flame temperature variation as a function of f/o can be estimated by assuming the reaction is adiabatic and isobaric. Thus, the total change in enthalpy $\Delta H = 0$ and the adiabatic flame temperature can be calculated by the following equation [6]:

$$\Delta H_{rxn}(T_i) + \int_{T_i}^{T_f} C_p^{products}\, dT = 0 \quad (2)$$

where T_f and T_i are the adiabatic flame temperature and ignition temperatures, respectively. Only the heat capacity, C_p, of the products is needed due to the assumption that the reaction is considered to be instantaneous. Thus, any heat generated from the reaction only goes into heating the products [6,7]. When C_p is considered to vary with temperature, T_f in Eq. (2) can be solved by numerical methods. The values of ΔH_f^o (enthalpy of formation at 298.15 K) and C_p used to calculate the adiabatic flame temperature are shown in Table 1.

The effects of combustion synthesis of the blue-emitting phosphor cerium activated yttrium silicate $(Y_{1-m}Ce_m)_2SiO_5$, whose luminescent properties were also being studied for potential use as the blue component for field emission display applications, were studied [8]. The structure of Y_2SiO_5 is isostructural to rare-earth (RE) oxyorthosilicates, written as $RE_2(SiO_4)O$, which exhibit two polymorphic monoclinic space groups dependent on the ionic radii of the RE ion [9,10]. Structure X_1-RE_2SiO_5 crystallizes for the larger rare-earths, La to Tb with space group $P2_1/c$, and X_2-RE_2SiO_5 for the smaller rare-earths, Dy to Lu with space group C2/c. When Y replaces the RE ion, Y_2SiO_5 can form a low temperature modification X_1-Y_2SiO_5 or high temperature modification X_2-Y_2SiO_5, depending on its preparation. The X_1 phase transforms to X_2 at ≈ 1190 °C and has a melting temperature of 1980 °C [11]. When Ce^{3+} replaces Y^{3+}, this material has a blue emission in both the X_1- and X_2-Y_2SiO_5 structures, shown in Fig. 1. The blue emission arises from electronic transitions from the 5d to either the $^2F_{5/2}$ or $^2F_{7/2}$ ground state of Ce^{3+} (shown in Fig. 1). More details on the emission properties of this phosphor can be found in [8,12,13].

2. Experimental procedure

2.1. Phosphor synthesis

The combustion synthesis of yttrium silicate is unique in that a non-nitrate compound, SiO_2, was used, as silicon nitrate does not exist. Instead, a suspension of fine particle size (≈0.014 μm) SiO_2 was used. This is the

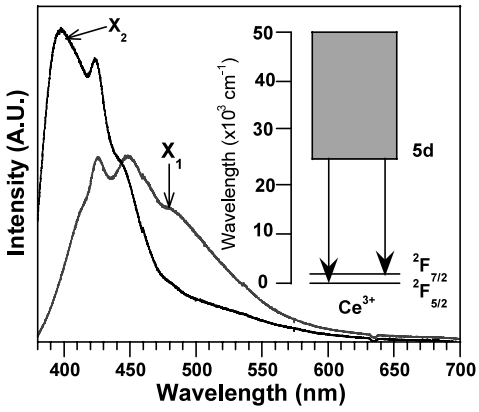

Fig. 1. The emission from the low temperature X_1-Y_2SiO_5 and high temperature X_2-Y2SiO5 structures of $(Y_{1-m}Ce_m)_2SiO_5$. Ce^{3+} energy level diagram adapted from Ref. [21].

first reported use of a solid suspension in a reaction solution. The starting materials were $Y(NO_3)_3{\cdot}6\ H_2O$ (Reacton, 99.99%, Alfa Æsar), fumed 0.014 μm SiO_2 (99.8%, Aldrich), $Ce(NO_3)_3{\cdot}5\ H_2O$ (Reacton 99.99%, Alfa Æsar) and carbohydrazide CH_6N_4O (98%, Aldrich). While other fuels were tried, only carbohydrazide produced powders with dramatic variations in powder properties as a function of f/o. Stoichiometric (f/o = 1.25), fuel lean (f/o < 1.25) and fuel rich (f/o > 1.25) mixtures were prepared. The f/o ratios studied are shown in Table 2.

The composition used in this study was $(Y_{0.98}Ce_{0.02})_2SiO_5$. Reactants were weighed and placed into 80 × 40 ml Pyrex vessels, along with 30 ml of deionized water. Reactants were dissolved and atomically mixed with a magnetic stirrer for 30 min. The reaction vessel was then put into a preheated muffle furnace at 500 °C and viewed through one of the open doors. After completion of the reaction, the powder was gently ground with an agate mortar and glass pestle for 2 min to break up the powder and then analyzed. A fraction of the powder was also annealed at 1350 °C for 1 h to transform it to the more luminescent X_2-Y_2SiO_5 phase.

Table 2
Fuel-to-oxidizer ratios for carbohydrazide

% From stoichiometric	Cardohydrazide (f/o)
−30	0.875
0	1.250
30	1.615
60	2.012
100	2.500

2.2. Characterization

The phases present and crystallite sizes were verified and calculated using X-ray diffraction (XRD) (Scintag, XDS 2000). Transmission electron microscopy (TEM) (Philips CM30, 300 keV) images were taken to accurately measure the crystallite sizes and phases present in individual particles. A laser scanning particle size analyzer (Horiba) and scanning electron microscope (SEM) (FEI Co., XL30 ESEM-FEG) were used to measure the particle size. Brunauer-Emmett-Teller (BET) (Quantachrome Instruments, NOVA series) analysis was performed to determine the specific surface area ($m^2\ g^{-1}$) and pore volume of the powders. Carbon–hydrogen–nitrogen (CHN) analysis was carried out to determine the amount of organic contaminants as a function of f/o. The combustion synthesis reaction was thermodynamically analyzed to predict the adiabatic flame temperature by Eq. (2). The cathodoluminescence (CL) emission intensity (cd m^{-2}) was measured using a spectroradiometer (CS-100, Minolta, NJ). Powders were excited at excitation voltages of 500–5000 eV at a constant 5 mW cm^{-2} of power (spot size 0.196 cm^2) and the efficiency (lumens/watt or lm/w) calculated by:

$$\varepsilon = \frac{\text{lm}}{\text{W}} = \frac{\pi \times \text{luminance (cd/m}^2) \times \text{spot size (m}^2)}{\text{volts} \times \text{amps}} \quad (3)$$

3. Results

Fig. 2 shows XRD scans for as-synthesized powders for each f/o studied, with the amount of fuel increasing from top to bottom and are compared to a standard (Nichia, NP-1047, PA). The first observation is that the

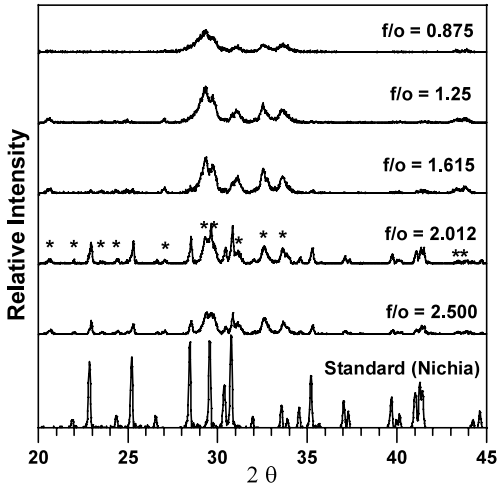

Fig. 2. XRD scans of as-synthesized powders made with different f/o ratios, compared with a standard. Asterisk denotes X_1-Y_2SiO_5 peaks.

suspension of SiO_2 is totally consumed by the reaction; Y_2O_3 and SiO_2 were not detected separately and only the two phases of Y_2SiO_5 are observed. It is presumed that SiO_2 undergoes a solid state reaction with Y_2O_3 to form Y_2SiO_5 from the tremendous heat generated by the surrounding fuel/nitrate reaction. Secondly, for the f/o = 0.875–1.615 (30% fuel rich to 30% fuel lean, respectively), these scans exhibit only the low temperature X_1-Y_2SiO_5 (JCPDS card No. 41-4 [14]) phase of this material. XRD also shows that the peaks narrow with increasing amount of fuel, indicating that the crystallite sizes are increasing. For f/o = 2.012 and 2.5 (60 and 100% fuel rich, respectively), these powders exhibit both the X_1-Y_2SiO_5 (* signify X_1 peaks) and X_2-Y_2SiO_5 (JCPDS card No. 36-1476) phases, with f/o = 2.012 exhibiting the largest crystallite sizes for combustion synthesized powders. The standard exhibits only the X_2-Y_2SiO_5 phase and has the largest crystallite sizes. Table 3 displays the crystallite sizes calculated using Scherrer's formula and the phases present in each f/o.

Fig. 3(a, b) show scanning electron micrographs of the typical particle morphologies from (a) as-synthesized powders produced by the combustion synthesis reaction and (b) the particle morphology after the powder has been annealed at 1350 °C for 1 h. The as-synthesized particles exhibit a plate-like morphology with a high amount of agglomeration and porosity. The porosity is produced by the superheated gases escaping from the reaction. Particle size analysis showed that the mean particle size of all powders produced at different f/o was 11.4 ± 6 μm, with sizes ranging from 1 to 50 μm [15]. To achieve the highest luminescent efficiency for this phosphor, as-synthesized powders are annealed at 1350 °C for 1 h. The particles exhibit a matrix of necked crystallites (0.2–0.5 μm in size), with particles still having a large degree of porosity and agglomeration with a similar particle size and range of the as-synthesized powders. The morphology of the industrial standard of this phosphor was observed to have elongated spherical particles ≈5 μm in size and exhibited only a few 1–3 μm size crystallites necked together.

Table 3
Calculated crystallite size from XRD data using Scherrer's formula, measured crystallite size from dark field TEM images and the phases present in each powder

f/o Ratio	XRD crystallite size (nm)	TEM crystallite size (nm)	Phase
0.875	31	13	X_1
1.250	44	18	X_1
1.615	56	36	X_1
2.012	23/110	19/83	X_1/X_2
2.500	47/80	64 (mixed phases)	X_1/X_2
Standard*	173	≈3 μm	X_2

X_1 low temperature phase; X_2 high temperature phase.
* Nichia, NP-1047, PA.

Fig. 4(a, b) are TEM bright field images of particles formed with a f/o = 2.012, showing the different morphologies obtained from this reaction. Fig. 5(a, b) and Fig. 6(a, b) show corresponding electron diffraction patterns and dark field images, respectively. Fig. 4 (b) shows a 'sponge'-like structure with a high degree of porosity. The dark field image in Fig. 6(b) reveals small crystallite sizes, ≈19 nm, which correspond to the measured crystallite sizes for X_1-Y_2SiO_5, ≈23 nm, in the XRD pattern (Fig. 2) for f/o = 2.012 (* peaks). The ratio of the ring diameters from these crystallites, shown in Fig. 5(b), confirm these crystallites are X_1-Y_2SiO_5. Fig. 4(a) shows well-defined, faceted crystals from the same f/o = 2.012. The dark field image of Fig. 6(a) shows the particle consisting of large crystallites, ≈83 nm in size. XRD from f/o = 2.012 (Fig. 2) revealed that large crystallites, ≈110 nm, correspond to X_2-Y_2SiO_5. Indexing of the pattern shown in Fig. 5(a) confirm these crystallites are X_2-Y_2SiO_5. Table 3 summarizes the crystallite sizes measured from TEM micrographs from each f/o ratio.

CHN and BET surface area analysis on each f/o studied are shown in Fig. 7. CHN analysis reveals that while the quantities of hydrogen and nitrogen were too small to be accurately measured, the weight percent of carbon shows a clear trend of decreasing with increasing f/o. The surface area is also seen to decrease with increasing f/o. The pore volume of the as-synthesized powders was also found to be influenced by the f/o, with results from BET porosimetry shown in Fig. 8 ($V(r)$ represents the volume of pores with radiuses between $r+dr$). The inset in Fig. 8 shows how the pore volume changes with pore radius for each f/o. The total pore volume is derived by integrating under each curve for each f/o. Fig. 8 shows that as the average pore radius increases with increasing f/o, the total pore volume decreases. The explanation is that as the reaction temperature increases, the crystallites grow causing the coalescences of smaller pores and leads to the coarsening of larger pores which are then eliminated through surface transport mechanisms. This analysis is limited by the BET in that pore radii larger than 25 nm are indistinguishable from the spacing between particles. Appendix A discusses the pore size analysis, in which an equation is developed to predict the specific surface area of porous powders from BET pore size data.

The adiabatic flame temperature was calculated using Eq. (2). The heat capacity, C_p^{products}, was considered to vary with temperature, and the ignition temperature was assumed to be 298 K due to the heat of formation only known at that temperature. O_2 was added either as a reactant (f/o > 1.25) or product (f/o < 1.25) to chemically balance the equations. The addition of O_2 was deemed reasonable since the reaction occurs in an open-

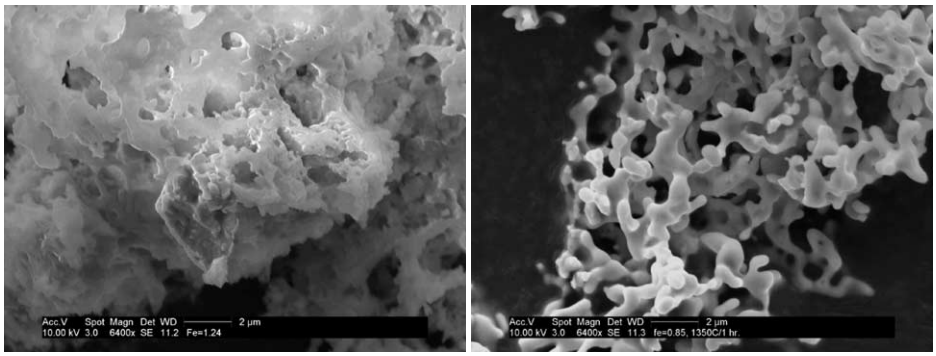

(a) (b)

Fig. 3. (a) Scanning electron microscopy of as-synthesized particles produced from a combustion synthesis reaction. (b) After the as-synthesized particles have been annealed at 1350 °C for 1 h.

air furnace. The flame temperature, T_f in Eq. (2), was determined numerically, with the results shown in Fig. 9, in which it increases with f/o. The extra oxygen added for fuel rich reactions helps to burn the excess fuel, increasing the flame temperature.

The f/o also had an indirect affect on the luminescent efficiency of the as-synthesized powders. Fig. 10 shows the luminescence efficiency as a function of acceleration voltage at the f/o studied. Powders made with f/o = 0.85 (30% fuel lean) and 1.25 (stoichiometric) were found to have negligible efficiencies due to these powders exhibiting the smallest crystallite sizes and largest amount of carbon contamination. Powders made with f/o $\geq$ 1.615 had measurable luminescence efficiencies due to their large crystallite sizes and least organic contamination. Regardless of the f/o ratio the powders were produced with, upon annealing the as-synthesized powders at 1350 °C for 1 h, the powders were found to exhibit comparable properties. The carbon contamination and surface area reached their minimum values while the luminescent intensity and crystallite sizes reached their maximum. The luminescent efficiencies of the annealed powders were also found to be comparable to the standard.

4. Discussion

The results from the analysis described above indicates that the flame temperature increases with increasing f/o ratio and reached a maximum when combustion reaction solutions were between 60 and 100% fuel rich. Though the reaction does not truly occur under adiabatic conditions, the calculation of the adiabatic flame temperature from Eq. (2) reinforces this result, as shown in Fig. 9. XRD and TEM both showed that as the f/o increased, the crystallite sizes also increased, reaching their largest sizes at f/o = 2.012 (60% fuel rich). For f/o = 2.5 (100% fuel rich), the crystallite sizes were found to decrease slightly, possibly due to the excess fuel not burning as efficiently, producing a lower flame temperature. XRD and TEM also confirmed that both

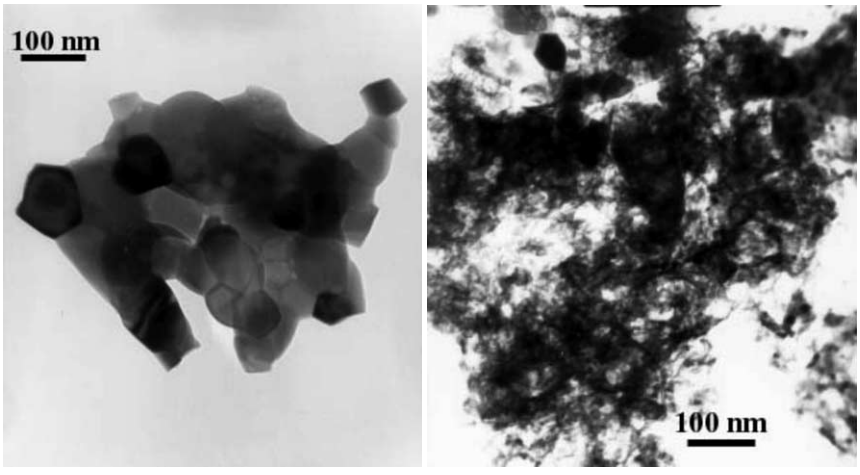

(a) (b)

Fig. 4. (a) TEM micrographs of bright field images for a f/o = 2.012 powder, (a) well defined crystallites and (b) 'sponge' structure.

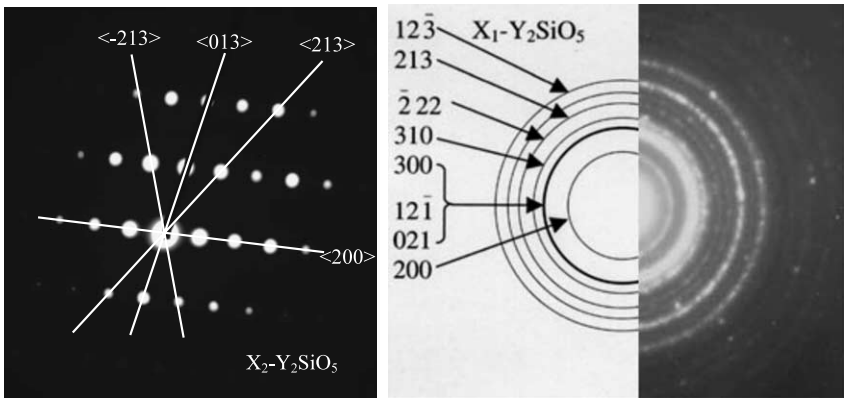

(a) (b)

Fig. 5. Electron diffraction pattern for (a) the particle shown in Fig. 4(a); and (b) for the particle shown in Fig. 4(b).

the X_1-Y_2SiO_5 and X_2-Y_2SiO_5 phases were produced and can occur together even from the same reaction, as shown for f/o = 2.012 and 2.5. Fig. 4(a, b) and Fig. 6(a, b) show that the two phases exhibit different particle morphologies, with X_1-Y_2SiO_5 having small crystallites in a spongy structure and X_2-Y_2SiO_5 having large crystallites in a less porous structure.

Powders produced with f/o = 2.012 and 2.5 exhibit both X_1- and X_2-Y_2SiO_5 phases, which is due to an inhomogeneous temperature distribution within the reaction area. During the combustion reaction, gases are being evolved while solid crystallites nucleate, grow and undergo a solid state reaction with the suspended SiO_2. Understanding of the kinetics of the reaction is thus more complex than that for either solid state or sol-gel methods. It is hypothesized that the kinetics of the crystal growth for f/o = 2.012 and 2.5 are that X_1-Y_2SiO_5 forms at the flame edge, where cooler temperatures would prevail, while the middle of the flame produces the hottest regions and would have exceeded the transition temperature ($\approx$ 1190 °C) long enough to nucleate and grow the X_2-Y_2SiO_5 phase. Thermodynamic modeling [15] of this reaction has shown that as the f/o increases, the mole fraction of gases produced also increases. The evolved gases, while superheated from the surrounding reaction, would also take heat away from the reaction, effectively reducing in the flame temperature. This is not the case for this reaction because of the presence of oxygen from the atmosphere. When O_2 is added as a reactant to Eq. (1), the excess O_2 reacts with the excess fuel, producing higher flame temperatures (as shown in Fig. 9) even though the increasing mole fraction of gases would tend to decrease the reaction temperature. The excessive temperature in the middle region would also facilitate faster growth, yielding larger crystallites than in cooler regions. Once the reaction has exceeded the transition temperature, growth of X_2-Y_2SiO_5 is at the expense of growth of X_1-Y_2SiO_5. Table 3 shows that for f/o = 2.012, the X_1-Y_2SiO_5 phase (23 nm) is smaller than that for f/o = 1.615

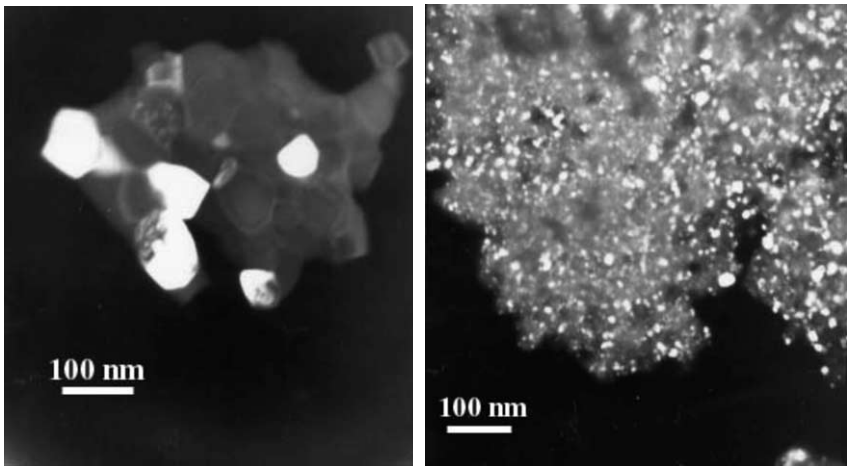

(a) (b)

Fig. 6. Dark field TEM micrographs of (a) particle shown in Fig. 4(a); and (b) particle shown in Fig. 4(b).

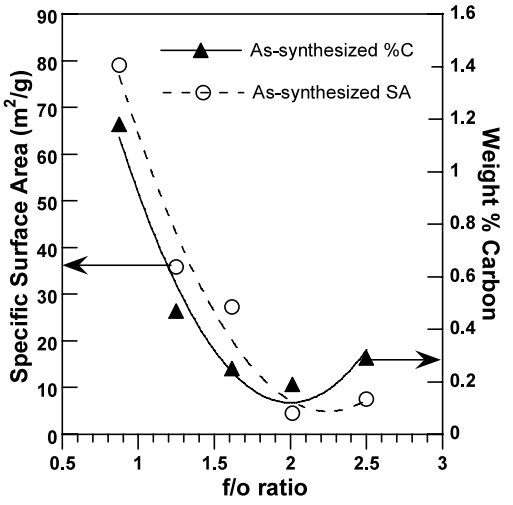

Fig. 7. Weight percent of carbon concentration and BET specific surface area (SA) as a function of the f/o ratio for as-synthesized powders.

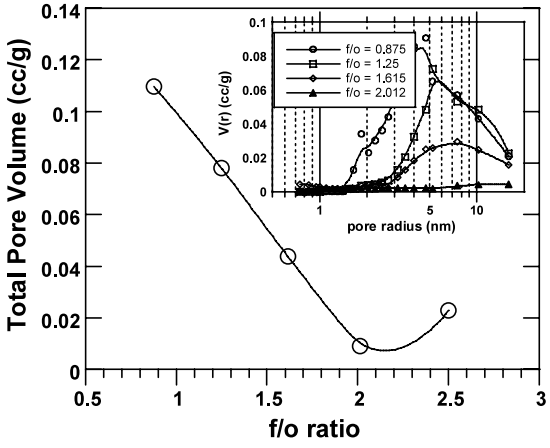

Fig. 8. Pore size distribution as measured by the BET for as-synthesized powders.

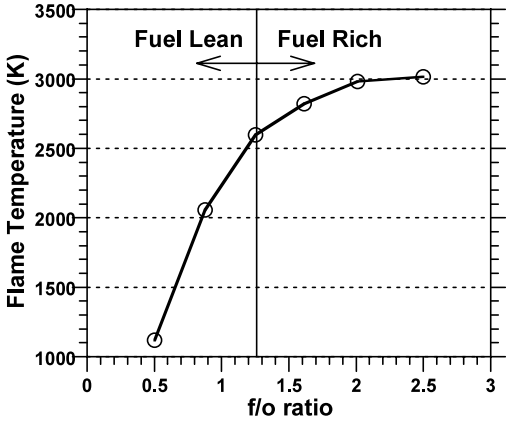

Fig. 9. Adiabatic flame temperature calculation for carbohydrazide using Eq. (2).

(56 nm), while for X_2-Y_2SiO_5 phase has a large crystallite size (110 nm). For f/o = 2.5, the X_2-Y_2SiO_5 crystallite size is smaller (80 nm) than f/o = 2.012 (110 nm), but the X_1-Y_2SiO_5 phase is larger (47 nm) than that for f/o = 2.012 (23 nm). Though TEM and XRD both show the presence of X_2-Y_2SiO_5 at f/o = 2.012 and 2.5, luminescence measurements show only emission from X_1-Y_2SiO_5, suggesting that only in a few locations did the reaction temperature become high enough to nucleate X_2-Y_2SiO_5. The observed differences in morphology may be from the inert gases escaping faster from the hotter regions, allowing the particles to grow large crystallites with very little gas being trapped to create the porosity. In cooler regions, the slower growth kinetics would allow the gas to create more porosity, as shown in Fig. 8.

Carbon contamination and surface area were found to decrease with f/o, reaching a minimum at f/o = 2.012, which indicates the flame temperature increasing with increasing f/o. Typically, carbon is liberated from powders by annealing them at high temperatures in an oxidizing environment. While the amount of carbon in the precursor solution increases with increasing f/o, the subsequent increase in the flame temperature more efficiently consumes the carbon, leaving smaller amounts of organic contamination in the powders. BET and CHN both show a slight increase in surface area and carbon contamination, respectively, at f/o = 2.5 (100% fuel rich) and support the result that the highest flame temperature was achieved with f/o = 2.012 (60% fuel rich) mixture.

Organic contaminants and crystallite sizes impact the luminescent efficiency of phosphor powders. As crystallite sizes increase, more activator ions are located in crystallographic sites that promote radiative emission and are further from defects, such as grain boundaries

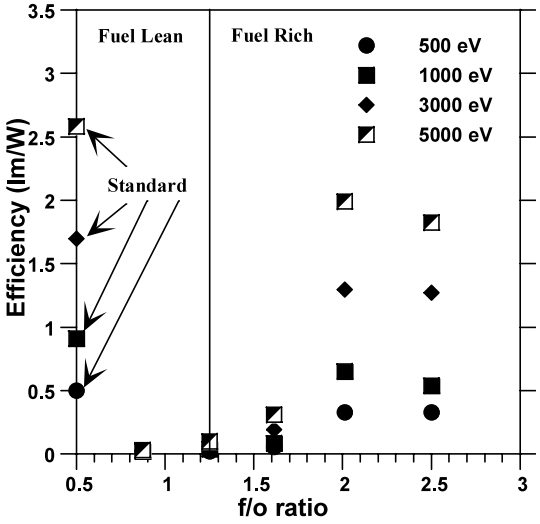

Fig. 10. Efficiency of as-synthesized powders as a function of the f/o ratio.

and the particle surface. These defects quench luminescence by allowing the incident energy to be non-radiatively emitted, such as by phonon emission. Contaminants, such as carbon, also allow the incident energy to be non-radiatively emitted at these contaminate sites, decreasing the phosphor efficiency. Thus, to achieve high efficiency phosphors, it is important that the crystallite sizes be large to decrease the number of defects and be of high chemical purity. Details of the effect of defects on the luminescent efficiency can be found in Ref. [16]. The impact of these types of defects on the luminescent efficiency of this phosphor can be seen in the as-synthesized powders.

The highest luminescent as-synthesized powders were produced with f/o = 2.012 and 2.5; these powders having the lowest carbon contamination and largest crystallite sizes. While XRD and TEM showed that these f/o ratios exhibited both phases, only emission from X_1-Y_2SiO_5 was observed, with the efficiency reaching a maximum at f/o = 2.012. Though with a f/o = 2.012, smaller X_1 crystallites were formed than with f/o = 2.5, the higher carbon contamination with f/o = 2.5 quenched the luminescence and decreased the efficiency to slightly below that with f/o = 2.012 (Fig. 10). The high carbon concentration with f/o = 1.615 greatly lowered the efficiency of these powders. To achieve efficient luminescence, these phosphors were all annealed at 1350 °C for 1 h. The effects of the combustion synthesis on the as-synthesized powder were then no longer observed in the annealed powders, with the luminescent efficiencies and physical properties all found to be comparable.

5. Conclusions

The effects of combustion synthesis on the physical and luminescent properties of blue-emitting $(Y_{0.98}Ce_{0.02})_2SiO_5$ were investigated. To the best of these authors' knowledge, for the first time, a fine particle solid, SiO_2, was suspended in combustion reaction solutions, where as only metal nitrates and fuels have been used previously to create a multicomponent oxides. The reaction totally consumed SiO_2, producing only Y_2SiO_5. Fuel-to-oxidizer ratios <1.615 were found to form only the low-temperature X_1-Y_2SiO_5, while f/o ratios ≥ 1.615 were found to exhibit both the low temperature X_1-Y_2SiO_5 and high temperature X_2-Y_2SiO_5 phases. While the crystallite size was found to increase with increasing f/o ratio, the carbon contamination and specific surface area were both found to decrease with increasing f/o ratio. This suggests that the flame temperature of the reaction was increasing with the f/o ratio, with the highest flame temperature being achieved for f/o = 2.012. The luminescent efficiency of the as-synthesized powders were also found to be a maximum at f/o = 2.012. Calculation of the adiabatic flame temperature confirmed that the flame temperature should increase with increasing f/o ratio. The total pore volume was found to decrease with increasing f/o ratio, while the average pore size was found to increase. An equation was developed to predict the specific surface area from Brunauer–Emmett–Teller data for porous particles. It was shown to better predict the surface area compared to the equation that only takes into account spherical, fully dense particles. Finally, annealing powders, made with any f/o, at 1350 °C for 1 h eliminated the effects of combustion synthesis, producing a highly luminescent phosphor that can be used in display applications.

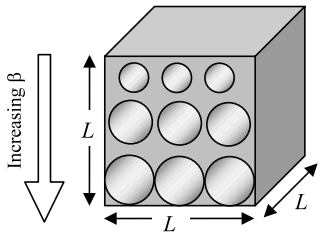

Fig. 11. Diagram of cubic particle used to predict the specific surface area. Here, $n = 3$ and shows how $\beta = r/L$ increases with larger pore size. The last row is the limiting case, where all pores of radius r touch.

Acknowledgements

The authors would like to acknowledge the financial support of the Phosphor Technology Center of Excellence by DARPA Grant No. MDA972-92-1-0030 and the National Science Foundation, Grant No. DMR9972509. The authors also wish to thank Dr Lauren Shea Rohwer and Professor Lea Rudee for their many helpful discussions. We also acknowledge partial support from the Materials Corridor Initiative (Contract No. 00-01-205-6) and the technical work performed by F. Ruiz and G. Vilchis from the CCMC, Ensenada, Mexico.

Appendix A

An equation is developed that relates the specific surface area to the diameter of the particles. For spherical, fully dense particles, the specific surface area ($m^2\ g^{-1}$) can be estimated by [17]:

$$SA = \frac{3}{\rho r} = \frac{6}{\rho L} \tag{A1}$$

where ρ is the density of the material and L is the diameter of the particle. When particles are porous and not spherical, this equation no longer gives a reasonable estimation of the surface area. The new equation is based on the diagram shown in Fig. 11. Particles are

considered to be cubic with sides of length L and having cylindrical pores of radius r that are regularly spaced and periodic and run the length L of the cubic particle. The following equations were used to derive the predicted specific surface area (SA_p):

$$\text{Volume of cube:} \quad V = L^3 - \pi r^2 L n^2 \tag{A2}$$

$$\text{Surface area of cube:} \quad S = 6L^2 + 2\pi r L n^2 - 2\pi r^2 n^2 \tag{A3}$$

$$\text{Specific surface area:} \quad SA = \frac{S}{m} = \frac{S}{\rho V} \tag{A4}$$

where n represents the total number of pores counted along a particular direction of the cube. For the volume of the cube, the volume of the cylindrical pores ($\pi r^2 L n^2$) is subtracted from the total volume of the cube. For the surface area, the surface area of the walls of the cylindrical pores ($2\pi r L n^2$) is added, while the area of the ends of the pores ($2\pi r^2 n^2$) is subtracted. Eq. (A2) and Eq. (A3) are substituted into Eq. (A4) to yield:

$$SA_p = \frac{(6L^2 + 2\pi r L n^2 - 2\pi r^2 n^2)}{\rho(L^3 - \pi r^2 L n^2)} \tag{A5}$$

Making the following substitution, $\beta = r/L$, Eq. (A5) simplifies to:

$$SA_p = \frac{(6 + 2\pi\beta n^2 - 2\beta^2 n^2)}{\rho L(1 - \pi\beta^2 n^2)} \tag{A6}$$

When the particles are fully dense ($n = 0$, no porosity), Eq. (A6) reduces to the equation that would be derived for fully dense cubic particles:

$$SA_p = \frac{6}{\rho L} \tag{A7}$$

Eq. (A6) now takes into account the open porosity of powder samples. While particles probably exhibit some closed porosity, open porosity is only taken into account here since most particles in this study exhibited the 'sponge' structure shown in Fig. 4(b).

To use Eq. (A6) for the specific surface area prediction, the following must be known: the pore radius, r (measured by BET), the volume of the sample (V_s), the sample weight (m), the number of cubic particles in the sample (α), the size of the particles (L) which was determined by a particle size analyzer, the pore volume (V_p) (measured by the BET) and the number of pores (n).

The variables above are either calculated or measured by the BET. The first step in using Eq. (A6) is to calculate the number of model particles (α) (or cells) in the sample used by the BET. A known amount of sample (m) is put into the BET. The volume of the sample is then simply calculated by:

$$V_s + \frac{m}{\rho} \tag{A8}$$

α is then calculated by:

$$\alpha = \frac{V_s}{V_c} \tag{A9}$$

where V_c is the volume of the model cell (simply $L \times L \times L$). It was assumed that the particle volume was just the particle size cubed as measured by particle size analysis. Next, the number of pores, n, can be determined by the following equation:

$$\pi r^2 L n^2 \alpha = V_p m \tag{A10}$$

V_p is the pore volume measured by the BET and is given as ($m^3\ g^{-1}$) and is multiplied by the sample mass, m, to obtain a value for the pore volume. The mean pore radius, r, is calculated by the BET (Fig. 8). The value for β is calculated by dividing the pore radius, r, by the length of the model cell, L. With β, n, L and r now known, Eq. (A6) can now be used to predict the specific surface area of a porous powder sample. Due to the limitation of the BET, Eq. (A6) could only be used to determine the specific surface area for the following f/o ratios = 0.875, 1.25 and 1.615. Fig. 12 shows the measured specific surface area, the predicted specific surface area using Eq. (A6) and the predicted specific surface area using Eq. (A1).

Fig. 12 shows that Eq. (A6) predicts the specific surface area better than Eq. (A1). The reasons that Eq. (A6) does not better predict is due to the particles not being cubic and the porosity not being cylindrical, as assumed in the model above. The morphology of combustion synthesized particles is more plate-like, which would cause the predicted value to deviate somewhat from the measured value. Eq. (A6) does

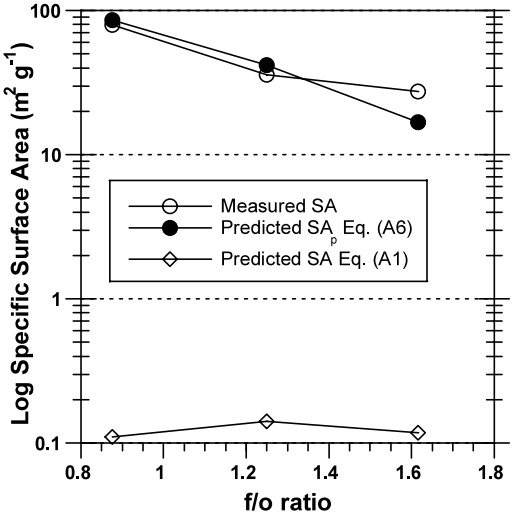

Fig. 12. Plot of the measured surface area compared to the predicted surface area by Eq. (A6) and Eq. (A1).

predict the specific surface area to at least the same order of magnitude, while Eq. (A1) was off by two orders of magnitude.

References

[1] J.J. Kingsley, K.C. Patil, Mater. Letts. 6 (1988) 427–432.
[2] Y. Zhang, G.C. Stangle, J. Mater. Res. 9 (1994) 1997–2004.
[3] K.R. Venkatachari, D. Huang, S.P. Ostrander, W.A. Schulze, J. Mater. Res. 10 (1995) 748–755.
[4] L.E. Shea, J. McKittrick, O.A. Lopez, J. Am. Cer. Soc. 79 (1996) 3257–3265.
[5] J. McKittrick, L.E. Shea, C.F. Bacalski, E.J. Bosze, Displays 19 (1999) 169–172.
[6] J.H. Noggle, Physical Chemistry, Harper Collins, New York, 1996, pp. 281–286.
[7] C.H.P. Lupis, Fundamental Principles and Equations for a Close System, Elsevier Science, New York, 1983, pp. 2–10.
[8] E.J. Bosze, G.A. Hirata, L.E. Shea-Rohwer, J. McKittrick, J. Lum. (2003) (in press).
[9] M. Leskelä, J. Suikkanen, J. Less-Common Metals 112 (1985) 71–74.
[10] J. Reichardt, M. Stiebler, R. Hirrle, S. Kemmler-Sack, Phys. Stat. Sol. (a) 119 (1990) 631–642.
[11] J. Wang, S. Tian, G. Li, F. Liao, X. Jing, Mater. Res. Bull. 36 (2001) 1855–1861.
[12] R.Y. Lee, F.L. Zhang, J. Penczek, B.K. Wagner, P.N. Yocom, C.J. Summers, J. Vac. Technol. B16 (1998) 855–857.
[13] J. Lin, Q. Su, H. Zhang, S. Wang, Mater. Res. Bull. 31 (1996) 189–196.
[14] JCPDS, Joint Committee on Powder Diffraction Standards: International Centre for Diffraction Data (ICDD), 12 Campus Blvd., Newtown Square, PA 19073.
[15] E.J. Bosze, J. McKittrick, G.A. Hirata, L.E. Shea, in: C.R. Ronda, K.C. Mishra, L. Shea, A. Srivastava, H. Yamamoto (Eds.), Physics and Chemistry of Luminescent Materials, vols. 99-40, Electrochemical Society Symposium Proceedings, USA, 1999, pp. 174–184.
[16] L. Ozawa, Cathodoluminescence: Theory and Application, Kodansha, Tokyo, 1990.
[17] J.W. Evans, L.C. DeJonghe, The Production of Inorganic Materials, Macmillan, New York, 1991, pp. 125–127.
[18] Dow Chemical Company Thermal Research Laboratory, Joint Army, Navy, Air Force Thermochemical Tables, Clearinghouse for Federal Scientific and Technical Information, Springfield, VA, 1965.
[19] J. Liang, A. Navrotsky, T. Ludwig, H.J. Seifert, F. Aldinger, J. Mater. Res. 14 (1998) 1181–1185.
[20] D.R. Gaskell, Introduction to the Thermodynamics of Materials, Taylor and Francis, Washington, DC, 1995, p. 546.
[21] T. Kano, Principal phosphor materials and their optical properties, in: S. Shionya, W.M. Yen (Eds.), Phosphor Handbook, CRC Press, New York, 1999, pp. 177–200.